THE ASTRONOMICAL JOURNAL VOLUME 113, NUMBER 5 MAY 1997

THE GIANT, GAS–RICH, LOW-SURFACE–BRIGHTNESS GALAXY NGC 289[1]

WILFRED WALSH[2]

School of Physics, University of New South Wales, NSW 2052, Australia, and Australia Telescope National Facility, CSIRO, P.O. Box 76, Epping, NSW 2121, Australia
Electronic mail: wwalsh@atnf.csiro.au

LISTER STAVELEY-SMITH AND TOM OOSTERLOO

Australia Telescope National Facility, CSIRO, P.O. Box 76, Epping, NSW 2121, Australia
Electronic mail: lstavele@atnf.csiro.au, toosterl@atnf.csiro.au

Received 1996 September 26; revised 1996 December 26

ABSTRACT

Using Australia Telescope Compact Array neutral hydrogen and Anglo-Australian Telescope optical observations, we investigate the distribution of luminous and dark matter in the giant, gas-rich, low-surface-brightness galaxy NGC 289. The observations show NGC 289 to have a high H I-to-stellar mass ratio ($M_{\rm H\,I}/M_* \approx 0.4$), and an extremely large H I radius (70 kpc, or $\sim$13 disk scale-lengths), making the H I velocity field an excellent probe of a galaxy dark halo to an unusually large radius. Between $\sim$10 kpc and 30 kpc the rotation curve dips by 14% of the maximum velocity. Warped disk and spiral density wave models are investigated to explain this dip and to determine the cause of significant velocity deviations in the vicinity of the H I spiral arms. The best-fit kinematic model has $M/L_I = 2.1\ M_\odot/L_\odot$ for the stellar disk, only slightly lower than the maximum disk value of 2.3. A dark matter halo of $3.5\times10^{11} M_\odot$ is present, which is $\sim$3.5 times as massive as the combined stellar and gaseous components at the last measured point on the rotation curve. © *1997 American Astronomical Society.* [S0004-6256(97)01404-0]

1. INTRODUCTION

There are now numerous observational lines of evidence corroborating the existence of quantities of dark matter around galaxies (see Ashman 1992 for a review). One of the clearest pieces of evidence for dark matter halos comes from the rotational velocities of the extended H I disks of spiral galaxies. Among such galaxies, there appears to be an inverse dependence of dark matter content on optical luminosity (Tinsley 1981; Broeils 1992; Persic & Salucci 1988; Ashman *et al.* 1993), leading to the suggestion that the dark-to-luminous matter ratio may be a crucial parameter determining the Hubble sequence.

At present, however, detailed dark matter parameters are poorly known in many cases, with estimates of the central density for the same galaxy, as determined by different authors, varying by well over an order of magnitude (cf. Kent 1987; Broeils 1992; Barnaby & Thronson 1994; Sackett *et al.* 1994). The reasons for this uncertainty are many, and include: the distance uncertainty, the uncertainty in the mass-to-light ratio of stellar disk, bulge and halo populations, that the 3D form of these populations are unknown, that many disk galaxies are not pure axisymmetric systems but often participate in interactions and/or suffer from bars, warps, and other structural features, and that the problem of finding a mass distribution that accounts for the observed kinematics usually has more than one plausible solution (Lake & Feinswog 1989).

In an attempt to reduce some of these uncertainties and further explore some of the fundamental correlations between dark matter halo parameters and other galaxy parameters, we have defined a sample of late-type galaxies for which we have obtained high-quality H I rotation curves with the Australia Telescope Compact Array (ATCA). This paper describes the results of a study of our first object, the nearby spiral galaxy NGC 289. NGC 289 is unusually gas–rich and, with a very extended low-surface-brightness disk, falls squarely into the new class of giant low-surface-brightness (LSB) spirals identified by Sprayberry *et al.* (1995b). In terms of gas-richness, NGC 289 is more extreme than any in the Sprayberry *et al.* sample and, although the properties of NGC 289's exponential disk are not well defined, the disk clearly satisfies their "diffuseness index" for LSB disks. NGC 289 is thus an excellent candidate for studying the distribution of luminous and dark matter in a massive, late-type, LSB galaxy. We briefly discuss previous work on NGC 289 in Sec. 2, and discuss the most likely value of its distance in Sec. 3. The radio and optical observations are described in Sec. 4 and the results (structure of the H I and optical disk, gas kinematics) are discussed in Sec. 5. Mass models are discussed in Sec. 6.

2. PREVIOUS STUDIES OF NGC 289

Early sky-survey plates show NGC 289's bright nucleus and inner $3.6' \times 2.5'$ disk only. Later plates (e.g., UKST/

[1]Based on observations with telescopes of the Australia Telescope National Facility and the Anglo-Australian Observatory.
[2]Current address: Radioastronomisches Institut der Universitat Bonn, Auf dem Hügel 71, D-53121 Bonn, Germany.

 0004-6256/97/113(5)/1591/16/$10.00

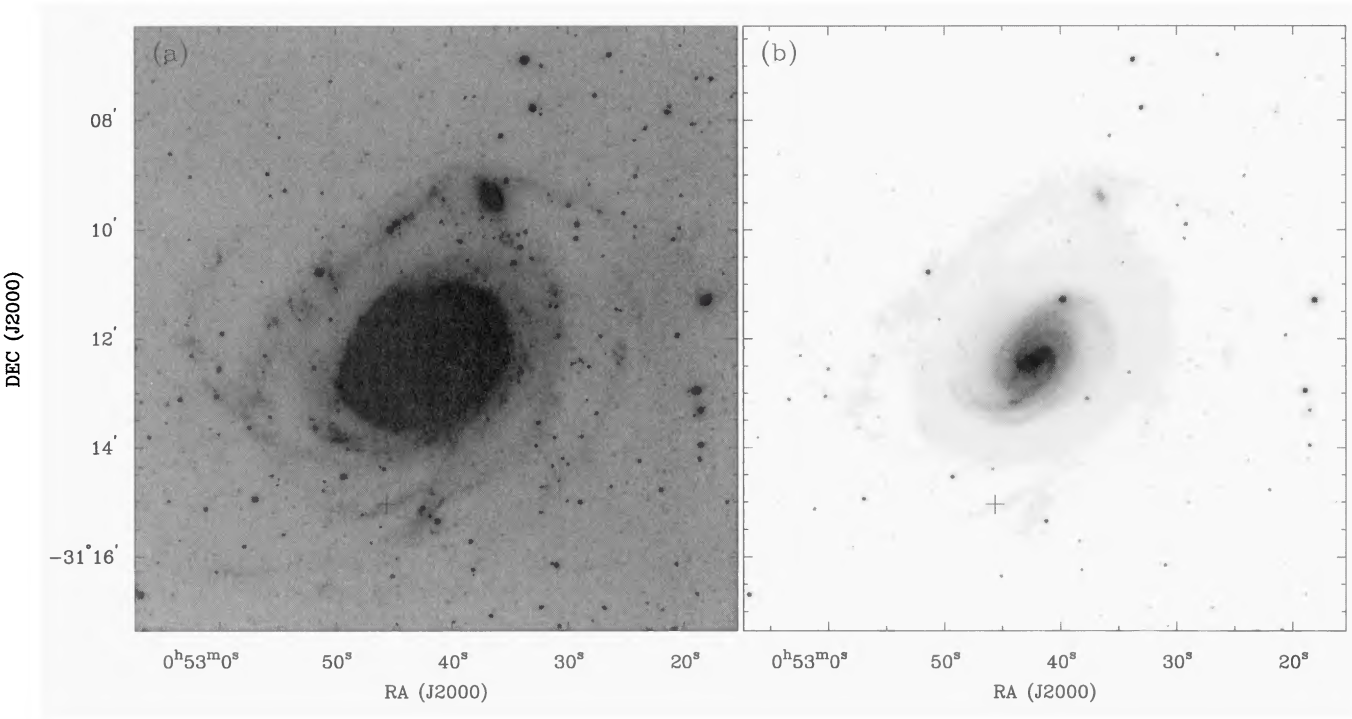

FIG. 1. NGC 289 as seen in the *V* band (Cousins filter) with the AAT using square root (a) and logarithmic (b) transfer functions. A dwarf companion can be seen 3.′3 north of the nucleus.

SERC *J* survey) revealed NGC 289's faint outer arms and led to revised disk sizes of up to $\sim 11' \times 7'$. Colors have been measured by Véron-Cetty (1984) and Buta & Williams (1995). Vorontsov-Velyaminov (1977) includes NGC 289 in his catalog of interacting galaxies and Arp (1981) obtains redshifts of 1426 km s^{-1} (absorption) and 1574 km s^{-1} (emission) for NGC 289, and 1510 km s^{-1} in emission for the dwarf companion 3.′2 north of NGC 289's nucleus, and notes that the "low surface brightness, presumably Im-type companion is obviously interacting with the arms in the north." However, inspection of our CCD data (Fig. 1) and a $V-I$ image suggest that the companion is a dwarf elliptical rather than an irregular.

Pence & Blackman (1984, hereafter PB), observing Hα and [N II] lines, found the relative nuclear emission line strengths to be consistent with photoionization resulting from H II regions throughout the galaxy, and noted that such emission in NGC 289 was much fainter than that in comparable spirals in their study. Véron-Cetty & Véron (1986) obtained optical spectra of NGC 289's nucleus in the 400–700 nm range, classifying it as a composite of an H II region and a Seyfert. The [N II], Hα, and [S II] lines were detected; Hβ, [O I], and [O III] were not. Bica & Alloin (1987) and Bonatto *et al.* (1989) performed absorption and emission-line spectroscopy of NGC 289's nucleus, which they classified as "weak-lined." The internal reddening due to inclination was found, by comparison with nearly face-on template galaxies with similar nuclear stellar populations, to be $E(B-V)=0.10$.

NGC 289 was detected by the *IRAS* satellite and, with fluxes of $S_{12\ \mu m}=410$ mJy, $S_{25\ \mu m}=770$ mJy, $S_{60\ \mu m}=6.07$ Jy, $S_{100\ \mu m}=16.64$ Jy, was classed by Devereux (1987) as infrared-luminous, though its far-infrared colors are normal for a late-type spiral galaxy.

Fouqué (1984) used the Nançay Radiotelescope to establish an H I diameter of 9.′1 for NGC 289 which is less than half that seen with the ATCA (Sec. *5.2*). Radio continuum images have previously been published by Condon (1987) and Unger *et al.* (1989). Both images are low-resolution, showing an extended central concentration of emission and a 17 ± 1 mJy, unresolved feature in the southern spiral arm (at $\alpha = 00^h52^m45.6^s, \delta = -31°15\prime 03$,J2000).

3. DISTANCE TO NGC 289

Several distance determination methods have now been applied to NGC 289, the results of which are listed in Table 1. Buta & de Vaucouleurs (1983) use inner ring structures of 453 disk galaxies as a distance indicator to place NGC 289 at a distance of 30.3 Mpc, which disagrees considerably with values obtained from the angular diameter considerations of Sandage (1993) who obtains 38.0 Mpc, and Bottinelli *et al.* (1986) who apply the revised *B*-band Tully-Fisher relation to get 16.7 Mpc. Using our best estimate of the corrected total blue magnitude [$B_o^T = 10.83$ cf 11.29 in The Third Reference Catalog of Galaxies (de Vaucouleurs *et al.* 1991, hereafter RC3)] and V_m taken from Table 6 we obtain a distance of 13.7 Mpc using this technique. We note that Sprayberry *et al.* (1995a) find the Tully–Fisher relationship to be less trustworthy for LSB galaxies and, in particular, that large LSB galaxies tend to be over-luminous for their rotation speeds.

The heliocentric velocity of NGC 289, determined in Sec. *5.4* is $cz = 1628$ km s^{-1}. Correcting for solar motion in the Local Group (following the IAU convention), and using the Hubble relation with a constant of $H_0 = 75$ km s^{-1} Mpc^{-1}, we find a distance to NGC 289 of 21.7 Mpc. If we further account for Virgocentric flow using a model in which the

TABLE 1. Distance estimates for NGC 289.

Method	Distance (Mpc)	Reference
Tertiary Indicators	22.4	de Vaucouleurs (1979)
Redshift Distance[a,b]	19.4	Tully (1988)
Redshift Distance[c]	21.0	Kraan–Korteweg (1986)
Redshift Distance[a,d]	21.0	This paper (adopted)
Angular Diameter	38.0	Sandage (1993)
Inner Ring Structure	30.3	Buta & de Vaucouleurs (1983)
Revised B-band TF Relationship	16.7	Bottinelli *et al.* (1986)
Revised B-band TF Relationship[e]	13.7	This paper

[a]Using $H_0 = 75$ km s^{-1} Mpc^{-1}.
[b]Corrected for motion of the local group and Virgocentric infall of 300 km s^{-1}.
[c]Corrected for Virgocentric motion with local infall motion towards Virgo of 440 km s^{-1} and distance to Virgo of 21.7 Mpc.
[d]Corrected for Virgocentric infall–see text.
[e]Using our corrected total blue magnitude and our kinematically derived inclination and rotation velocity.

recessional motion of the Virgo cluster is 1296 km s^{-1} and the local infall motion towards Virgo is 250 km s^{-1}, we obtain a distance of 21 Mpc. NGC 289 is in a small group of galaxies consisting of NGC 254 (over a degree away) and ESO411-G26 (Maia *et al.* 1989), and we do not expect any significant peculiar velocities to be generated locally to the galaxy. In this paper therefore, we adopt the kinematic distance of 21 Mpc which agrees closely with the 22.4 Mpc adopted by PB on the basis of work described in de Vaucouleurs (1979).

4. OBSERVATIONS

4.1 Optical Observations and Calibration

Photometric images in the Cousins V and I bands were taken with the $f/1$ camera at the prime focus of the Anglo–Australian Telescope (AAT) (Fig. 1 and Table 2). The detector was a 1024×1024 Thomson CCD array with a pixel size of 0.″98. The exposure times were 600 s for V and 900 s for I, and the seeing was ~2″. Initial optical calibration was done using FIGARO and image processing was done using IRAF.

The bias current, estimated from an unexposed strip of the CCD, was subtracted from each image. The frames were flat-fielded using the median of several scaled twilight exposures. Photometric calibration was based on E-region standard stars (Graham 1982) and, for individual stars, is accurate to ±0.02 mag in V and to ±0.05 mag in I. These uncertainties are dominated by the aperture and airmass corrections. Extinction coefficients were measured to be 0.21 mag airmass^{-1} in V and 0.15 in I. All of the standard stars were observed at an airmass of 1.45, or less, and the galaxy was observed at an airmass of 1.05, or less. Vignetted regions were removed from the images and bright stars and the northern companion galaxy were replaced with a measure of the surrounding sky level plus noise.

The sky brightnesses, estimated from entire-image pixel modes, were 20.80±0.01 mag arcsec^{-2} in V and 18.60±0.01 mag arcsec^{-2} in I. The uncertainty quoted for the sky level, which derives from the uncertainty in establishing entire-image pixel modes plus a readout noise contribution, is in fact likely to be dominated by less well-defined 2D background estimation errors. As NGC 289 fills much of the CCD, the accuracy of the flat-fielding was investigated by applying the same sky-estimation technique to blank field images. Analysis of the residuals after sky subtraction suggest that the sky background is well determined out to a radius of about 450″, which appears to be beyond the detectable extent of NGC 289's disk and that brightnesses down to about 27 mag arcsec^{-2} can be measured.

Ellipse fitting to the inner regions revealed the bar, but was not possible in the vicinity of the inner spiral arms or in the shallow outer disk regions. Ellipses were fitted successfully to the I image at radii of 50″−200″. Average geometric parameters ($P.A. = 126°$, $i = 44°$) were used in IRAF tasks ELAPERT and POLYPHOT to define elliptical rings over which the surface brightness was measured by averaging counts in annuli of 10″ width. The radial luminosity profile thus obtained is shown in Fig. 2.

The integrated radial surface brightness profiles give total magnitudes of $V_T = 10.38 \pm 0.07$ mag and $I_T = 9.58 \pm 0.07$ mag (Table 2). Corrections for foreground and internal absorption based on RC3 values for Galactic and internal extinction were applied. We use Rieke & Lebofsky's (1985) Galactic extinction passband conversions to estimate A_I and A_V from A_B, and note that the Galactic extinction near the South Galactic Pole (NGC 289 lies at $b = -85.9°$) is poorly known (Burstein & Heiles 1982). Giovanelli *et al.* (1994) favor a higher value for A_I, but the difference is negligible for a galaxy as close to face on as NGC 289. The corrected magnitudes are $V_T° = 10.14$ and $I_T° = 9.35$ mag. For com-

TABLE 2. Optical observations of NGC 289 (AAT $f/1$ CCD Camera).

Property	V	I
Total magnitude, X_T	10.38 ±0.07	9.58 ±0.07
Corrected total magnitude,[a] $X_T°$	10.14	9.35
Isophotal diameter, D_{25}	5.′2	5.′6
Isophotal diameter, D_{26}	3.′9	
Isophotal axis ratio, R_{25}	0.69	0.69
Disk scale length,[b] α^{-1}	0.′88	
Central disk surface brightness' μ (mag arcsec^{-2})	20.0 ±0.7	19.0 ±0.7

[a]Corrected for Galactic absorption ($A_V = 0.02$, $A_I = 0.01$), as well as for internal extinction ($A_i = 0.22$).
[b]Adopted scale length. See text.

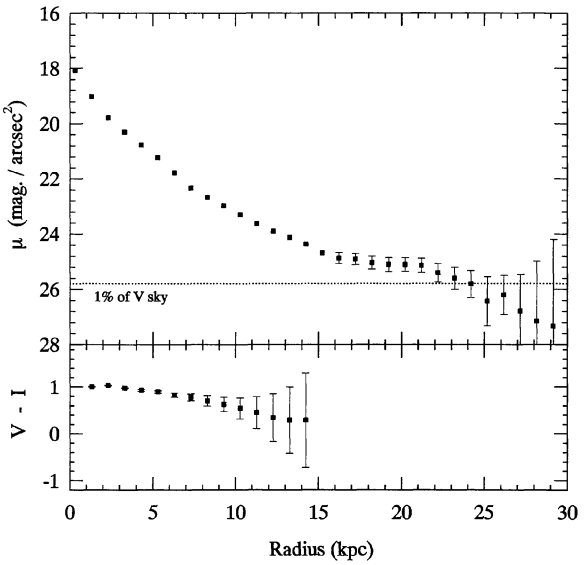

FIG. 2. Surface brightness profile in V and radial $V-I$ color profile of NGC 289.

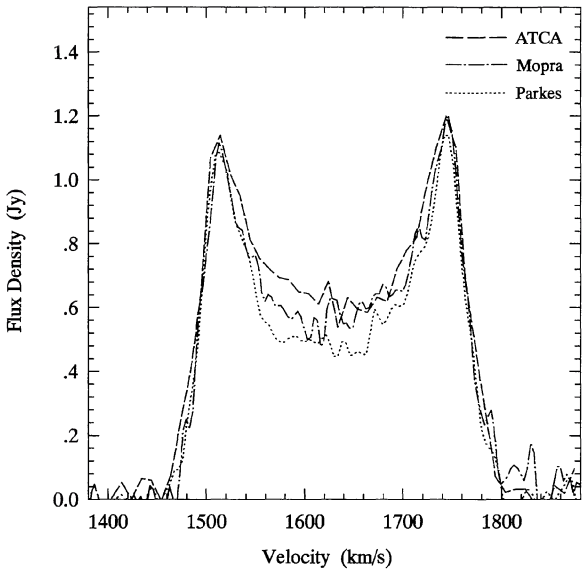

FIG. 3. Spatially integrated ATCA and Parkes 64 m spectra of NGC 289, with a Mopra single pointing observation. No flux has been resolved out in the ATCA observations. The velocity scale is heliocentric.

parison, RC3 lists $B_T=11.72$ and Lauberts & Valentijn (1989) list 11.36 which transform to $V_T=10.99$ and $V_T=10.63$ mag, respectively, when the RC3 value of $(B-V)_T=0.73$ is used. Both values are dimmer than ours. Given the photometric accuracy of our data, it seems likely that the previous magnitude estimates fail to measure accurately the luminosity of the extended outer disk, which extends to nearly twice R_{25}.

The frames were astrometrically aligned to stars from the *Digitised Sky Survey* (Lasker *et al.* 1990) by suitable scaling, shifting and rotation. Astrometric alignment accuracy is about 1″, commensurate with the accuracy of this catalog.

4.2 Radio Observations

4.2.1 Single-dish observations

NGC 289 was observed in 1990 August with the Parkes 64 m telescope and again in 1993 December using the newly commissioned AT correlator. Twenty-five separate pointing centers were observed in a diamond-shaped grid centered on $\alpha=00^h52^m41.9^s, \delta=-31°12'19''$ (J2000). The grid spacing was 7′, which is less than half of the FWHP telescope beamwidth of 14.′7 at the observing frequency of 1.412 GHz, and each position was observed for 300 s. A bandwidth of 32 MHz was used with 1024 spectral channels in each of two polarizations, giving a FWHP resolution of 8 km s^{-1} after Hanning smoothing. Reference positions 1° east and west of NGC 289 were used for sky subtraction. The flux density calibrator was PKS B1934−638, with an assumed flux density of 14.9 Jy at 1.412 GHz.

To estimate the total flux density at each velocity, the data were spatially integrated and normalized by assuming the beam of the Parkes Telescope to be Gaussian with corresponding solid angle 2.08×10^{-5} sr. The spatially integrated spectrum is plotted in Fig. 3 on top of the primary beam-corrected ATCA spectrum. The Parkes data in Fig. 3 are smoothed to match the spectral resolution of the ATCA data. The total Parkes flux integral of 250±30 Jy km s^{-1} is slightly lower than the ATCA integral of 270±30 Jy km s^{-1}, but is consistent within the uncertainties and indicates that any large-scale component which the ATCA has resolved out is only a small fraction of the total neutral hydrogen content of NGC 289. NGC 289 was also observed with the Mopra 22 m radiotelescope (a single antenna of the same specifications as each of the six ATCA antennas) in 1993 July. One 20 min observation was made. The Mopra flux integral of 234±40 Jy km s^{-1} is also slightly lower than the ATCA integral, but still consistent within the uncertainties. The Mopra spectrum is also shown in Fig. 3. Previous total flux determinations by Staveley-Smith & Davies (1987) (195±31 Jy km s^{-1}), PB (152±8 Jy km s^{-1}), Reif *et al.* (1982) (244±8 Jy km s^{-1}), and Fisher & Tully (1981) (161±8 Jy km s^{-1}) were not spatially integrated and therefore represent underestimates.

4.2.2 ATCA observations

Four separate 12 h observations of NGC 289 were obtained with the ATCA (Australia Telescope 1992) between 1990 November 19 and 1991 July 19 using the five telescopes of the 3 km array, and a maximum baseline of 2.0 km. The main details of the observations are summarized in Table 3 and the observing and analysis methods follow those described in Ryder *et al.* (1995). The bandwidth used was 8 MHz, divided into 512 channels each covering 3.3 km s^{-1}, and centered on 1.412 GHz (corresponding to a heliocentric velocity of $cz=1785$ km s^{-1}). The primary ATCA calibrator, PKS B1934−638, for which a flux density of 14.9 Jy at 1.4 GHz was assumed, was observed before each 12 h run. These observations also served as the bandpass calibration.

Each 12 h observation consisted of alternate scans of 40 min on NGC 289 and 4 min on the phase and secondary amplitude calibrator PKS B0022−423 (flux density ~3.0 Jy

TABLE 3. AT compact array H I observations of NGC 289.

Property	Value
Configurations	4×12^h (2.0km, 2×1.5km, 0.375km)
α (J2000) pointing center	$00^h52^m41\overset{s}{.}9$
δ (J2000) pointing center	$-31°12'19''$
Velocity resolution of final cube	9.9 km s^{-1}
FWHP synthesised beam	$88''\times31''$ (9.0×3.1 kpc)
FWHP primary beam	$33'$
Channel map cell size	$8''\times8''$
Channel map area	$34\overset{'}{.}1\times34\overset{'}{.}1$
rms noise per map	1.5 mJy beam^{-1}

at 1.4 GHz). Several time ranges were deleted from the dataset because of interference so, with calibration and drive time, the total integration time on NGC 289 reduces to approximately 40 h. The individual UV databases were processed using the NRAO's AIPS package. Both linear polarizations for each of the 10 baselines for each data set were examined and edited for bad data. After amplitude, phase, and bandpass calibration, continuum subtraction of each database was carried out in the complex visibility domain by subtracting first-order, least-squares fits to the line-free channels on either side of the NGC 289 velocity range. The original integration period of either 10 or 15 s was extended to 60 s by averaging, without introducing time smearing. Doppler corrections were then applied to align the data sets in a common heliocentric reference frame, and the data were combined in the UV plane.

The data were averaged into groups of 3 channels (separation 9.9 km s^{-1} or 46.875 kHz). The individual planes in the data cube were CLEANed down to 5 mJy, or 1000 iterations (using a loop gain of 0.1), whichever came first. Only baselines shorter than 7.5 kλ were used to form the naturally weighted data cube, which has a FWHP resolution of $88''\times31''$. A Gaussian taper of 7×4 kλ applied to baselines shorter than $\sigma=10$ kλ was used to obtain a uniformly weighted cube which has a resolution of $48''\times24''$. The average noise, measured in emission–free regions of the 48 channels that encompass H I signal from NGC 289, is Gaussian in character, with a channel-averaged rms of 1.5 mJy beam^{-1} (0.33 K). This is higher than the 'theoretical' value of 1.0 mJy beam^{-1} (which is calculated without allowing for confusing sources in the beam). The 3σ detection threshold is therefore $\sim1.8\times10^{19}$atoms cm^{-2} for each channel in the final cube. The data cube was corrected for primary beam attenuation, and 30 channel maps from the cleaned cube with significant H I emission are shown in Fig. 4. The total emission in each channel was measured by manually selecting the region of emission, and the resultant spectrum is plotted in Fig. 3. The flux integral of 270 Jy km s^{-1} is adopted as the best measure of the total H I emission, giving a total H I mass (assuming optically thin gas) of 2.8×10^{10} $M_\odot$ for the adopted distance of 21 Mpc.

Moment maps (column density, intensity weighted mean velocity and velocity dispersion) were calculated from the naturally weighted data cube using the AIPS task MOMNT. For comparison, a Gaussian fitting technique was also used (AIPS task XGAUS), the results agreeing at the level of the fitting errors, except in the innermost region where the beam-smearing causes the spectra to become broad and non-Gaussian. In all subsequent discussion, we use the results of the moment analysis. The column density map is shown in Fig. 5.

5. RESULTS

5.1 Structure of the Optical Disk

Figures 1(a) and 1(b) show the V band image of NGC 289 using logarithmic and linear transfer functions, respectively, to show the central regions and also the faint outer disk. In Fig. 1(b) shows clearly the two innermost spiral arms joining to form a bar about 85″ in projected length, in the very center of which lies an irregular, high-surface-brightness nucleus. The innermost part of the nucleus appears to be divided by a dust lane. The two main spiral arms, which begin at a radius of about ~70″, are seen to bifurcate at 110″. The central, high-surface-brightness region, extending to a radius of ~100″, does not have the appearance of a typical galactic bulge, although the $(V-I)$ color appears to become more blue out to 200″ (Fig. 2). Beyond this radius, the color is not observed to change, within the uncertainties, although the point–to–point scatter may indicate that the uncertainties have been overestimated. If so, Fig. 2 suggests that NGC 289 exhibits a slight color gradient, in the same sense as seen in most other spiral galaxies (de Jong 1995).

Schlosser & Mucsculus (1984), using a Fourier analysis to determine the pitch and number of spiral arms in a sample of large spiral galaxies, found that NGC 289 is most likely composed of two spiral arms, while Buta (1995), studying NGC 289's "inner ring," classifies NGC 289 as being multiply armed. Elmegreen & Elmegreen (1987), who have classified spiral arm structures to track density waves and found a basic distinction between "grand design" and "flocculent" galaxies among their 12 spiral arm classes, regard NGC 289 as two–armed. Grand design galaxies are those with prominent density wave modes, and are observed to have two-arm symmetry, with long, continuous spiral arms. Such galaxies are generally larger than flocculent galaxies by a factor of ~1.5 and are more likely to be found in dense groups. The outer disk (Fig. 1(a)) is very faint (the average surface brightness in V between 150″ and 300″ is $\mu_{\rm outer}=26.1$ mag arcsec^{-2}), consisting of long, narrow, spiral arms. The arms do not form a particularly regular pattern, and it is difficult to assess their number or continuity. Beyond 2′, NGC 289's apparent two main spiral arms are somewhat irregular in both their sweep and composition. There is no unambiguous evidence of inner and/or outer rings in the isophotes. As noted by Arp (1981), the companion 3′.3 north of the nucleus appears to have disturbed the northern arms, and a very LSB extension to the outermost arm can be seen in the southwest.

Unlike many spirals, NGC 289's surface brightness profile is not well fitted by a combination of a central bulge and exponential disk (Fig. 2). NGC 289's profile is reminiscent of giant LSB galaxies such as 0052−0119 and 1300+0144 (Sprayberry *et al.* 1995b). These galaxies have concave profiles not well fitted by a bulge and a disk. The appearance of NGC 289's center indicates that the bulge component, if any,

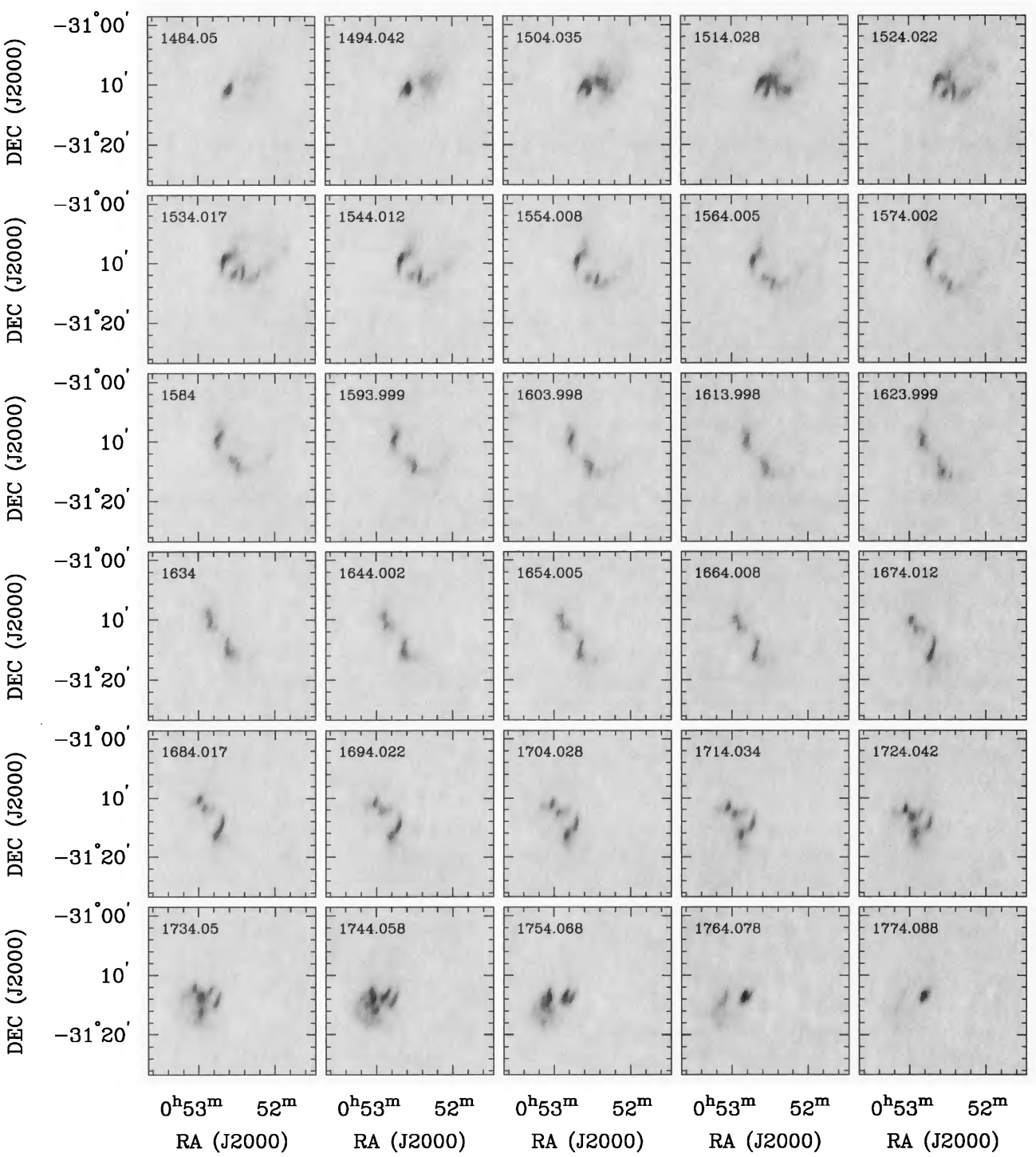

FIG. 4. 21 cm H I images of NGC 289 at heliocentric velocities ($c\Delta\lambda/\lambda_0$) between 1484 and 1774 km s^{-1}. Velocities are marked in the top left-hand corner of each plane. The greyscale dynamic range is −3 to 80 mJy/beam.

is very small or diffuse and, indeed, a de Vaucouleurs profile ($I=I_o e^{-(\alpha r)^{1/4}}$) provides a poor fit at all radii. A pure exponential disk ($I=I_o e^{-\alpha r}$) is a poor fit to the outer part of NGC 289's disk. For the purposes of comparison, formal parameters of a pure exponential disk fitted to the outer disk (in the region 8 to 28 kpc) are given in Table 2. Corrections for Galactic absorption, internal extinction and inclination have not been made to the central surface brightness of the disk fit.

The adopted scale length ($\alpha^{-1}=5.4$ kpc at the adopted distance) can be compared to an average of $3.3\pm0.3h^{-1}$ kpc for Kent's (1985) sample of Sa–Sd galaxies (measured in R), and $9.8\pm1.1h^{-1}$ kpc for the Sprayberry *et al.* (1995b) sample of giant LSB galaxies (measured in B). The extrapolated central surface brightness is estimated to be $\mu_I=19.0\pm0.7$ mag arcsec^{-2} and can be compared with the average value of $\mu_I=19.34\pm0.77$ mag arcsec^{-2} for a sample of Sc galaxies studied by Giovanelli *et al.* (1994).

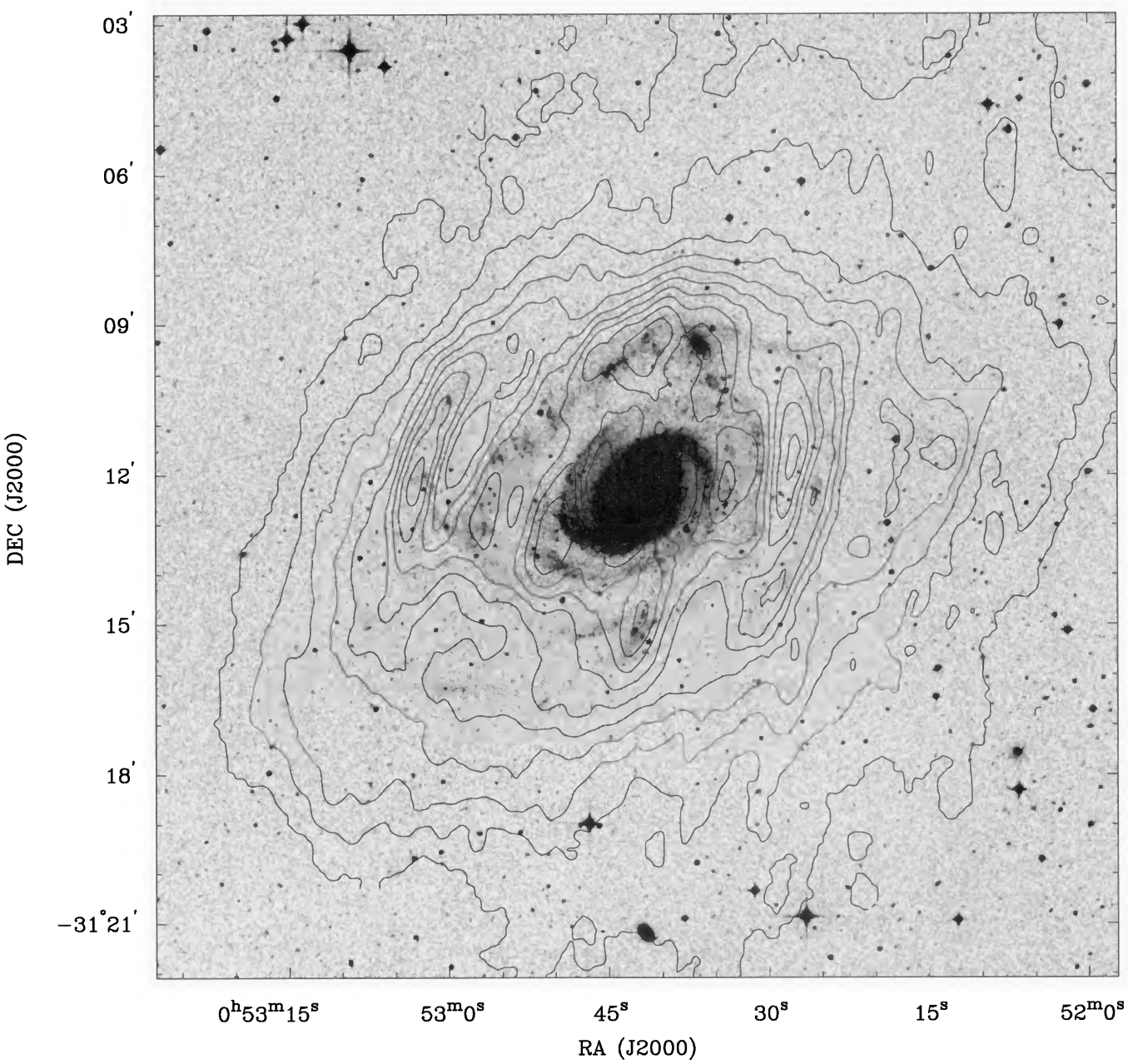

FIG. 5. Contours of H I column density in NGC 289 over the Digital Sky Survey image. Contours are at intervals of 1×10^{20} cm^{-2}, starting from 1×10^{19} cm^{-2}.

5.2 The Distribution of H I

The H I column density image, Fig. 5, shows the extremely large H I disk surrounding NGC 289. The disk is approximately elliptical, with the major axis aligned with both the optical and kinematic major axes. The 1×10^{19} atoms cm^{-2} contour extends $\sim22'$ along the major axis and $\sim15'$ along the minor axis. At the adopted distance, this corresponds to a radial H I extent of nearly 70 kpc. The H I extends well beyond the optical disk, which measures $9'\times6'$ at the 26 mag arcsec^{-2} isophote. For the adopted scale length for the stellar disk, this corresponds to an H I extent of 13 disk scale lengths. Such an extensive H I component, somewhat unusual for a grand design spiral, is comparable to low-luminosity objects such as DDO 154 (Carignan & Freeman 1988; Carignan & Beaulieu 1989), NGC 2915 (Meurer *et al.* 1996), NGC 3198 (Begeman 1987, 1989) and NGC 5963 (Bosma *et al.* 1988).

The H I distribution is clumpy, with pronounced maxima coincident with the inner and outer spiral arms and the V-shaped feature in the most southern spiral arm. The most striking feature of the H I distribution is the association of bright, regular H I arcs with the outermost optical spiral arms (Fig. 5). These H I arcs subtend, at a radius of $\sim300''$ from the nucleus, a projected position angle of 20° to 120° on the east side and 210° to 340° on the west side. These long and symmetrical arcs appear to be part of the outer spiral arms, but do not occur at the same radii on opposite sides of the center. The projected peak column density is 8.3×10^{20} atoms cm^{-2} in the eastern arc and 7.0×10^{20} atoms cm^{-2} in

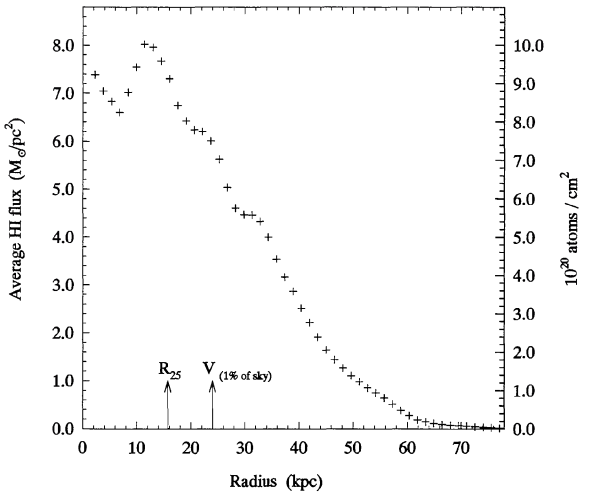

FIG. 6. Radial profile of deprojected H I surface density in NGC 289, from azimuthal averaging in concentric annuli with a constant inclination of 46° and constant position angle of 130°.

the western arc, and can be compared to the minima of $\sim 3.5\times 10^{20}$ atoms cm^{-2} in the contiguous interarm regions.

The radial distribution of H I in Fig. 6 was produced by averaging in concentric elliptical annuli, using the disk orientation parameters from the kinematical analysis (Sec *5.4*). The derived H I surface densities have been corrected for line-of-sight projection effects (assuming the gas to be optically thin) and plotted on a linear scale.

Our sensitivity limit is close to the interesting level of $\sim 2\times 10^{19}$ atoms cm^{-2} at which abrupt truncations are seen in the disks of M33 (Corbelli *et al.* 1989) and NGC 3198 (van Gorkom *et al.* 1993) and at which it has been suggested that H I can be ionized by extragalactic radiation (e.g., Maloney 1993; Corbelli & Salpeter 1993). At our sensitivity level, no sharp edge is seen in the disk of NGC 289, either in Fig. 6 or in deeper cuts made by stacking a few consecutive channels in regions of the disk with low velocity gradients.

The azimuthally averaged radial H I distribution shows a central deficiency of atomic H I, as is typical of disk galaxies. From a peak of 10.1×10^{20} cm^{-2} (~ 8 M$_\odot$ pc^2) at a radius of 12 kpc, the distribution declines linearly out to a radius of approximately 48 kpc, where the decline becomes slightly more gradual out to the limit of detectability at ~ 70 kpc (~ 2.7 Holmberg radii). The H I falls off more slowly than the light distribution, with the logarithmic azimuthally averaged density being almost flat to R_{25}, whereas the stellar disk declines approximately exponentially in that region (Figs. 6 and 2). Beyond R_{25} the H I density continues to decline more slowly than the extrapolated stellar disk. The density of the H I falls to 1M$_\odot$ pc^{-2} at a radius of 50 kpc, which is 3.1 times the radius at the blue 25 mag arcsec^{-2} isophote, compared to the average ratio for normal spirals which is 1.8 (Irwin 1995, and references therein) and 2.4 for LSB galaxies (van der Hulst *et al.* 1993).

5.3 NGC 289's Rotation Curve

The only previous kinematical study of NGC 289 is that of PB, who studied the gas dynamics of the inner 110″ (11 kpc at our adopted distance) using Hα and [N II] long-slit spectra with a velocity resolution of ~ 10 km s^{-1} to produce an 11″ rectangular grid of velocity measurements. The velocity field was found to be generally regular, exhibiting mainly circular rotation, although the alignment of the bar (P.A. 120°) with the major axis (P.A. 130°) and the fact that they observed few points within the bar region itself mean that their data are likely to overlook streaming motions. Some evidence of non-circular orbits was detected in the shape of the isovelocity contours and the non-perpendicularity of the major and minor kinematical axes. PB concluded that, as the difference between the observed velocities and their circular-rotation model were around 15 km s^{-1}, the dynamical effects of the bar were not very significant.

Figure 7 shows the velocity field determined from our first-moment H I image, with isovelocity contours at 10 km s^{-1} increments between 1510 km s^{-1} and 1760 km s^{-1} (the southern half has the higher velocities), superimposed on both the Digital Sky Survey image and the H I column density image. The velocity field displays the expected large-scale signature of an inclined, circular disk in differential rotation.

Figure 8, a single-beamwidth slice through the position–velocity data cube parallel to the major axis, shows that individual spectra have reasonably symmetric single peaks, except in the region near the center. Within a radius of 10 kpc the beam-smeared profiles are broad and non-Gaussian and the intensity-weighted mean and Gaussian fitting techniques diverge. Fortunately the PB data can be used to determine the rotation curve in this region. Figures 7 and 8 suggest that NGC 289 has a rotation curve resembling that of the Galaxy, with a steep central rise followed by a dip (Sec. *5.4*) before rising again to be approximately flat out to the last measured point.

To add the Hα data to our rotation curve, we reanalysed the raw PB data. For each data point, the observed radial velocity was converted to a rotational velocity using:

$$V(x,y)=V_{\rm sys}+V_{\rm rot}\cos\theta\sin i, \qquad (1)$$

where $V(x,y)$ denotes the radial velocity at rectangular sky coordinates (x, y), $V_{\rm sys}$ is the systemic velocity corrected for motion of the local group, $V_{\rm rot}$ is the rotational velocity, i is the angle of inclination, and θ is the azimuth measured from north to the receding major axis in the plane of the galaxy. We use the position of the dynamical center found in Sec. *5.4*. To minimize errors caused by large projection effects in the vicinity of the minor axis, points within 30° of the minor axis are excluded. The inclination was fixed at 45° and the position angle fixed at the value of 126° measured from isophotal fits; both values agree with PB's results. The approaching and receding sides were analyzed separately and the results averaged in 1.0 kpc-wide bins between 0.5 and 9.5 kpc. The results for the combined average of both sides are plotted in Fig. 11 as the triangular points with "error bars." The amplitudes of the "error bars" on either side of the data points shown are simply half the difference between the average value at each radius for the two sides, and are shown as indicative of the systematic uncertainties intro-

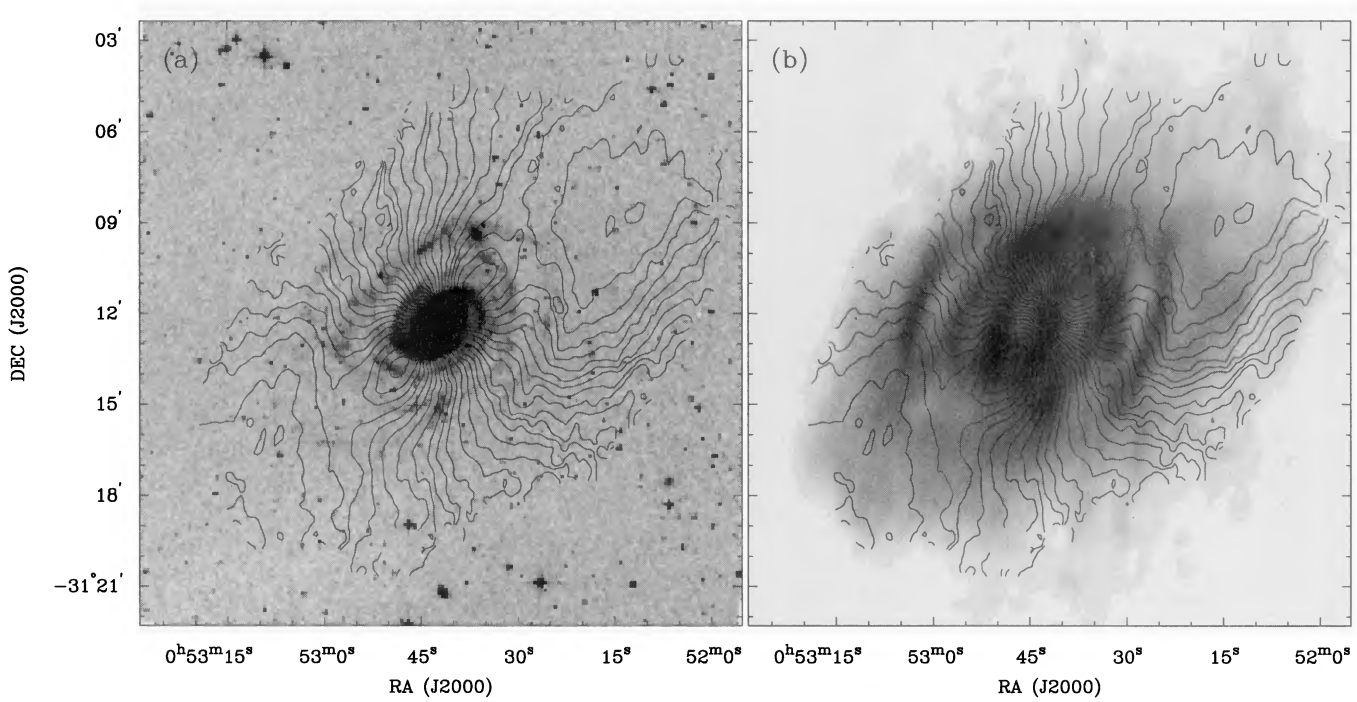

FIG. 7. Isovelocity contours of NGC 289 overlaid on the Digital Sky Survey photograph (a) and the column density map (b). The contour intervals are 10 km s^{-1}, (the southern half has the higher velocities) and the small cross indicates the position of the unresolved continuum feature (Sec. 2).

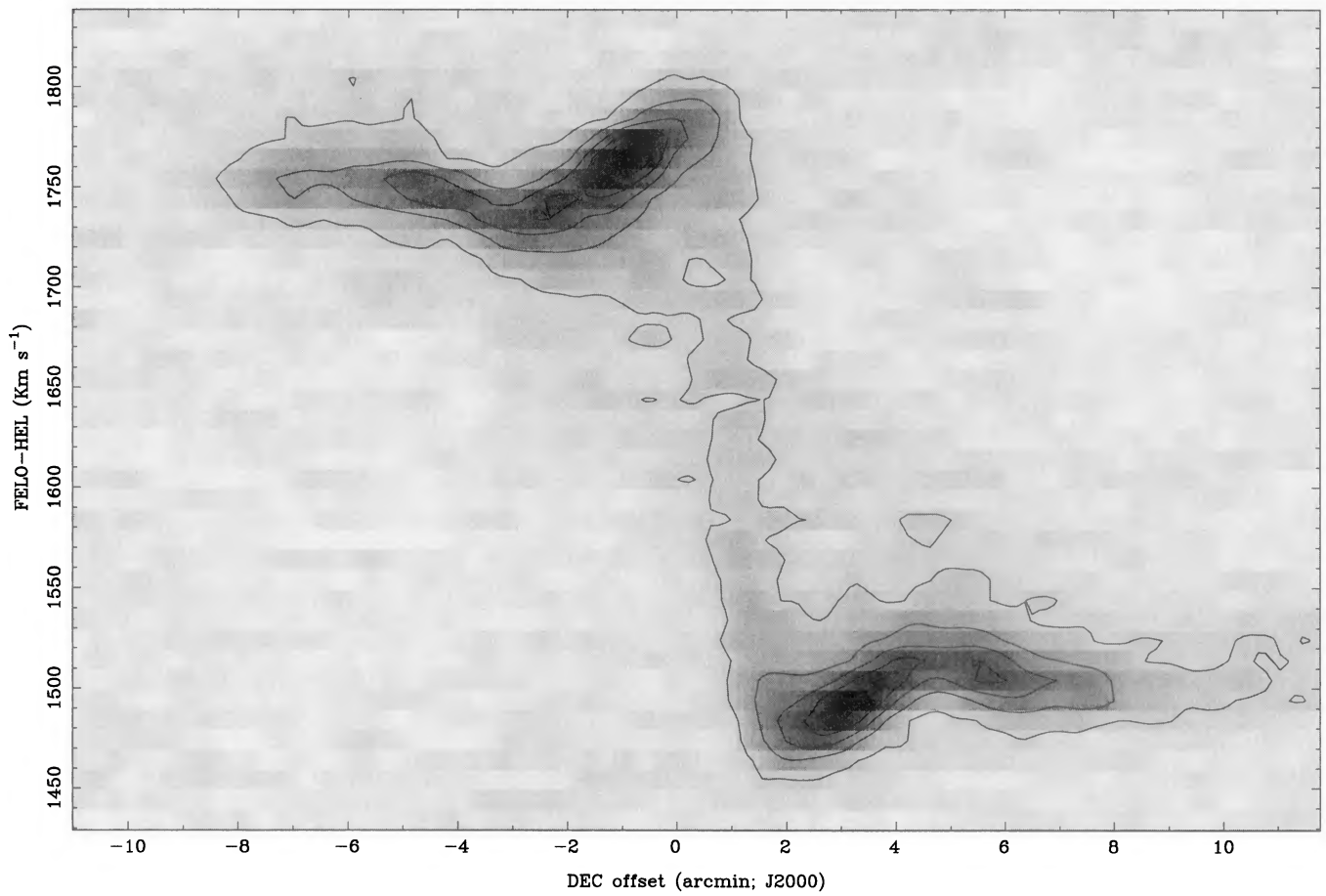

FIG. 8. Position–velocity diagram for NGC 289, using P.A. 130°.

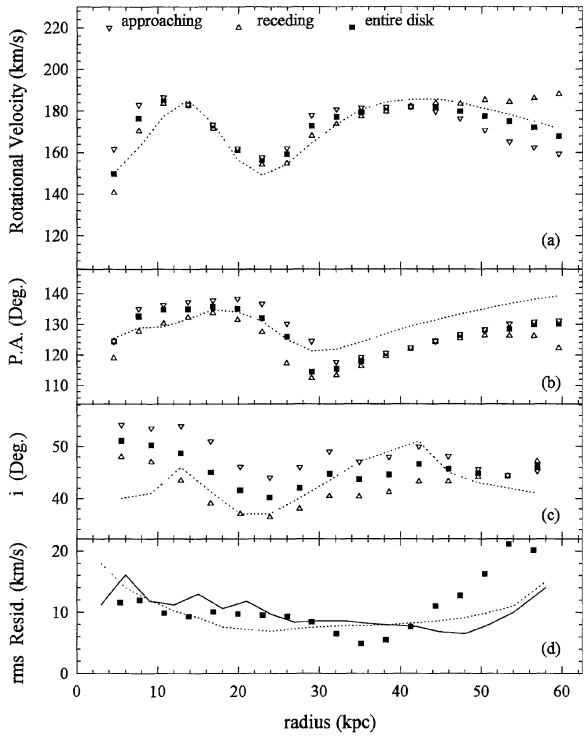

FIG. 9. Plot (a) shows the ROCUR-determined rotation curve for all disk points further than 30° away from the minor axis and with $\cos^2(\theta)$ weighting (solid squares) and, similarly, the rotation curve for the two halves of the galaxy (triangles). For the approaching and receding sides, no data points were excluded, but a $\cos^2(\theta)$ weighting was applied. The dotted line shows the rotation curve determined in a similar manner for the model velocity field incorporating a two-arm spiral density wave. Panels (b) and (c) show the observed position angle and inclination as a function of radius for the full disk (data points) and for the spiral density wave model (dotted line). Panel (d) shows the azimuthally averaged rms residuals (first–moment image – no density wave model) for the model velocity field generated for the full disk rotation curve with variable position angle and constant inclination (solid squares) and for the model velocity field incorporating the spiral density wave (dotted line) and for the warp disk model (solid line). See Sec. *5.4*.

duced by the assumption of circular symmetry. The maximum amplitude ($\sim$200 km s^{-1}) of the rotation curve derived in this way is considerably less than that derived by PB ($\sim$250 km s^{-1}), apparently because of the effect of excluding points near the minor axis.

To derive the kinematic parameters of the H I gas, we assume circular orbits in a disk of zero thickness coplanar with the stars and follow the method described by Begeman (1989): we use his algorithm as implemented in the AIPS task ROCUR. The procedure fits, by least-squares, inclined rings rotating in circular motion, to the velocity field, which we approximate with the first–moment image. The width of the rings is the mean of the uniformly weighted cube's beam, and the initial parameter estimates are taken from PB and ellipse fits to Fig. 1. Points within 30° of the minor axis are excluded and a $\cos^2\theta$ weighting is applied. We let ($\alpha_{\rm kin}$, $\delta_{\rm kin}$) mark the position of the rotation center of each ring and first solve for $V_{\rm sys}$, $\alpha_{\rm kin}$, $\delta_{\rm kin}$, $V_{\rm rot}$, i and θ, simultaneously. We find that the kinematic center of the H I disk of NGC 289 lies at $\alpha_{\rm kin}$(J2000) = $00^{\rm h}52^{\rm m}41\overset{\rm s}{.}9(\pm 25'')$, $\delta_{\rm kin}$(J2000) = $-\ 31°12'19''(\pm\ 15'')$ (precisely coincident with the center of the optical nucleus), with $V_{\rm sys} = 1628 \pm 2$ km s^{-1}.

TABLE 4. NGC 289 disk kinematic parameters.

Parameter	This study	PB
Rotation Center	0.″0±16″ E	0.0
(w.r.t. nucleus)	0.″0±16″ N	0.0
Position angle	130°±4°	126°±2°
Inclination	46°±5°	46°±10°
Systemic Velocity	1628±2km s^{-1}	1630±2 kms^{-1}

After fixing $V_{\rm sys}$, $\alpha_{\rm kin}$, and $\delta_{\rm kin}$ for every ring, numerous fitting strategies were attempted to estimate the variation of i, θ, and $V_{\rm rot}$ with radius. Coupling between parameters (especially inclination and velocity) makes a final choice of kinematic parameters somewhat subjective for NGC 289 (cf. Begeman 1989). The rotation curve shown in Fig. 9 was determined using an average value for the inclination (45°) with varying position angle. Fitting i, θ, and $V_{\rm rot}$ simultaneously results in a rotation curve with a slightly different shape, but within the errors, the maximum rotation velocity is the same and the outer part of the curve remains flat at the same amplitude. Between radii of 20 and 30 kpc the position angle undergoes something of a discontinuity, varying from 135° to 115°, and thereafter climbs towards $\theta = 130° \pm 5°$. This shift in position angle occurs at approximately the radius at which the bright H I arcs are seen but is also apparent in both the isophotes (Fig. 5) and velocity field (Fig. 7). Figure 9(b) shows how the position angle of each ring varies with radius.

We fit the full velocity field and the receding and approaching halves separately. In Fig. 9, triangles represent the two sides and the solid squares represent the entire disk solution. Additional support for the form of the adopted rotation curve comes from the position–velocity diagram (Fig. 8) and an inspection of the velocity field itself, where closing contours at radii of 120″ (12 kpc) and at 500″ (50 kpc) imply declining rotation speeds as seen in the rotation curve, given the assumption of constant inclination. Results of the tilted ring analysis are summarized in Table 4 and the rotation curve is listed in Table 6.

5.4 Warps and Spiral Structure in NGC 289

In Fig. 7, irregularities in the isovelocity contours reveal non-circular motions imposed upon the overall pattern of circular motion. Figure 7(b) shows the line of nodes twisting with respect to the major axis of the projected H I disk. The resulting deviation from circular rotation is approximately symmetric (under rotation by π) and is characteristic of both warped disks and spiral density waves. We now compare these two hypotheses.

H I warps are commonly observed beyond R_{25} in spiral galaxies (Briggs 1990; Bosma 1991), although no satisfactory explanation as to how long-lived, symmetric warps are generated and maintained has been developed (Binney 1992; Dubinski & Kuijken 1994). The tilted-ring analysis described in Sec. *5.3*, which allows each of i, θ, and $V_{\rm rot}$ to vary with with radius, shows that a warp of more than 20° is

TABLE 5. Kinematic model with spiral arms.

Parameter	Value
Density contrast,[a] c	0.80
Pitch angle, ψ	20°
Crossing Radius[b]	170″
Pattern speed, Ω_p[a]	40 km s^{-1} kpc^{-1}
Velocity Dispersion	12 km s^{-1}
Rotation Velocity[d]	170 km s^{-1}

[a]Density wave contrast after Rots (1974): $c=(\sigma_{max}-\sigma_{min})/2\sigma_{avg}$ with σ_{max}, σ_{min}, σ_{avg} representing the surface density in the arm, interarm, and azimuthal average, respectively.
[b]Radius at which the spiral pattern first crosses the major axis. Defines the phase of the spiral pattern.
[d]Amplitude of the (flat) model rotation curve.

required for an adequate description of NGC 289's kinematics. As in the case of the large warp in NGC 4013 (Bottema 1996), such a pronounced warp in NGC 289 creates the dilemma of how such a warp can both survive long enough to produce the approximately symmetric structures in the velocity field and not be smeared out by differential precession.

In Fig. 7(b), the column density shows a number of clumps in the inner 200″ possibly associated with the spiral arms or a ring. Close alignment of the kinks and bulges in the isovelocity contours, which indicate departures from circular rotation of up to about 30 km s^{-1}, with these and other overdensities in the H I column density is apparent. The kinks in the velocity contours in the outer part of the disk are clearly associated with the spiral arms.

As an alternative to the warp hypothesis, we model the gross radial features in NGC 289's kinematics using the linear SDW approach (Lin *et al.* 1969; Burton 1971) to compute the line-of-sight velocity components arising from the principal density wave mode. For a galaxy with as complex an appearance as NGC 289, we do not expect that this simplistic model, which considers only gas motions resulting from a single spiral mode and ignores the effect of the bar, the companion and nonlinear gas-dynamical processes, will be able to fit in detail the distortions apparent in the velocity field. Our approach is to model the observed non-axisymmetric motions.

TABLE 6. Deprojected rotational velocities in NGC 289.

Radius (″)	V_{rot} (N+S) (km s^{-1})	V_{rot} (N) (km s^{-1})	V_{rot} (S) (km s^{-1})
45	149.73	161.88	139.99
75	176.35	182.34	170.71
105	184.81	184.65	183.05
135	182.85	181.50	181.98
165	172.38	171.96	169.94
195	161.26	161.65	160.65
225	156.44	159.79	154.10
255	159.13	163.07	153.20
285	172.66	170.73	159.63
315	177.13	176.47	166.38
345	179.29	177.01	173.98
375	180.65	179.58	178.24
405	181.89	179.32	180.66
435	181.63	179.06	183.80
465	179.69	176.08	183.15
495	177.35	170.48	185.25
525	174.93	164.46	184.87
555	172.01	161.66	183.38
585	167.79	158.45	182.18
615	157.99	156.43	163.13
645	157.54	156.75	166.65
675	166.15	159.10	188.96
705	165.10	163.65	179.00

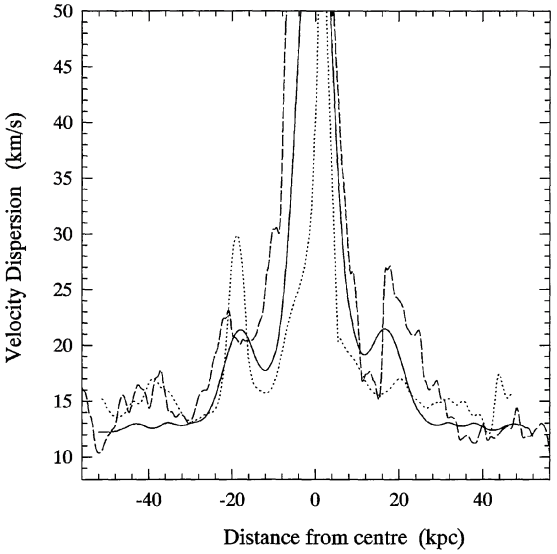

FIG. 10. Velocity dispersion as a function of radius. Slices along the major axis of the second–moment image (dashed line) and the velocity dispersion image generated from Gaussian fits to each spectrum (dotted line) are compared to the beam–smeared velocity dispersion expected for a model galaxy with 12 km s^{-1} velocity dispersion and spiral density waves as described in Table 5 (solid line). Within ~10 kpc from the center the beam crosses the minor axis. The left side of this plot corresponds to the northern side of the galaxy.

The inputs to our model, listed in Table 5, include a flat rotation curve, moderate density contrast and arms modelled as a logarithmic spiral with pitch angle 20° and suitable phase determined by trial and error. We explore the parameter space using constraints on the density contrast implied by the H I observations, and limits suggested by disk dynamics and results from other galaxies for the pattern speed and pitch angle (Binney & Tremaine 1987 and references therein).

We subject the model data cube (Table 5) to the same moment analysis used on the observed data and also determine the radial trend in the kinematic parameters for the model galaxy in the same way as was done for NGC 289. The velocity dispersion along the major axis is shown for both real and model data galaxies in Fig. 10. For NGC 289, these slices are obtained from the second–moment image (dashed line) and from Gaussian fitting to individual spectra (dotted line). They are compared with the beam–smeared velocity dispersion computed from the second-moment image of the model data cube generated with constant 12 km s^{-1} velocity dispersion (solid line). The trend and amplitude of velocity dispersion along the major axis of the model cube approximates the trends seen in the data. Figure 10 suggests that, while the radial trend in velocity dispersion is somewhat uncertain for the complex velocity structure seen in

NGC 289, the assumption of constant velocity dispersion is consistent with the data.

Figure 9(a) shows the rotation curve observed (solid data points) together with that derived from the velocity field for the adopted SDW model (dotted line) using the parameters listed in Table 5. The model's rotation curve shows a striking similarity to the observed rotation curve. In particular, the "hump" in the rotation curve at 12 kpc is well reproduced, as is the dip at 22 kpc. That such features in the apparent rotation curve are not necessarily the result of a peculiar mass distribution has been discussed by Lindblad & Lindblad (1994). Fridman (1994) reports that at least half of a sample of 25 well-studied spirals with prominent arms exhibit "velocity jumps" of greater than 10% in their rotation curves. In our model, the sudden radial change in NGC 289's position angle lags the dip in the rotation curve, in the manner observed. The amplitude of the position angle is not well fitted beyond the dip.

Curiously, we find that the only SDW model data cubes that agree with the data are those that result from *leading* spiral patterns. Evidence for leading spiral arms in other galaxies has come from studies of the azimuthal distribution of light and dust or from 2D Fourier analyses of spiral structure (e.g., Pasha 1985; Beckman & Cepa 1990; Buta *et al.* 1992; Walterbos 1994). Puerari & Dottori (1992) found both chaotic (NGC 1313) and regular (NGC 1566) spirals that consist of a mixture of leading and trailing modes. Byrd *et al.* (1993) are able to reproduce numerically a long-lived, leading, single arm spiral pattern when a low-mass companion makes a close retrograde pass by a halo-dominated disk galaxy. However, in the case of NGC 289 we do not see the expected signature of a density wave in the H I density images (Fig. 5 and Fig. 7, cf. Toomre 1983) and therefore cannot conclude that our SDW model provides good evidence for the presence of a leading spiral density wave mode. We also note that the assumed form of the observed rotation curve rests on the assumption of constant inclination.

Figure 9(d) represents azimuthally averaged rms velocity residuals for the full disk, no-density-wave model velocity field with variable position angle and fixed inclination (solid squares, Sec. *5.3*), for the warped disk model (solid line) and for the SDW model velocity field (dotted line). Within 10 kpc the SDW wave model, which does not consider the bar, is a poor fit to the data. Over most of the disk the average rms residuals in both the warped disk and SDW models are ≤ 12 km s^{-1} which is comparable to the average line-of-sight velocity dispersion (Fig. 10). Beyond 48 kpc the azimuthally-averaged residuals for both models increase up to 22 km s^{-1}. Inspection of the residual images after subtracting the model velocity fields suggests that a large-scale distortion in the outer half of the disk in the northeast causes the residuals to rise at large radii. In this region, the residuals are approximately 1.5 times the azimuthal average at that radius, the kinematic minor axis departs from kinematic major axis perpendicularity by 30° and the optical spiral arms appear to be distorted by an interaction with the companion galaxy.

Figure 9 suggests that the warped disk model is a reasonable model for the overall behavior of NGC 289's disk, but the kinks in the isovelocity contours seen in Fig. 7 show that is not the whole story. The SDW model's parameter space is large and, in NGC 289, the data do not constrain a unique set of parameters or determine individual parameters to better than about 30%. Since the H I column density image does not provide any evidence for a leading SDW in NGC 289, our SDW model cannot claim to represent the true state of the density wave in NGC 289. With an inclination always less than 55°, and a data cube with velocity resolution of 10 km s^{-1}, NGC 289 is too face-on for our H I data to allow us to come to a firm conclusion about the shape of the rotation curve. This limits our ability to model the dynamical state of NGC 289's disk and therefore we are unable to determine the relative contributions of the warp and the SDW to the observed kinematics.

TABLE 7. Effect of disk thickness.

z_0 kpc	z–law	M/L[a]	M_{disk}[b] (10^9 $M_\odot$)
0.0	···	1.8	55.4
0.5	exponential	2.0	61.6
0.5	sech–squared	1.9	58.5
1.0	exponential	2.3	70.8
1.0	sech–squared	2.1	64.7
1.5	exponential	2.5	77.0
1.5	sech–squared	2.3	70.8
2.0	exponential	2.8	86.2
2.0	sech–squared	2.5	77.0

[a]Assuming the maximum disk hypothesis.
[b]Cumulative mass of the stellar disk at R_{max}.

6. MASS MODELS

Since the asymmetries in the velocity field produce average data–model velocity residuals of not more than 12% of the maximum rotation speed (Sec. *5.4*), we now assume that NGC 289 is sufficiently axially symmetric for a rotation curve to provide a meaningful probe of the gravitational potential. We follow the method described in Broeils (1992), and references therein.

As neither the CCD images (Fig. 1) nor the radial surface brightness profile (Fig. 2) shows clear evidence for a stellar bulge component in NGC 289, we model the rotation curve with just a thick stellar disk, a thick gaseous disk and a spherical halo of "dark matter." The rotation arising from the gas is obtained from Fig. 6, scaled by 1.3 to allow for helium, and we use the I band surface brightness profile to represent the stellar disk.

For the vertical density law, we use both an exponential distribution, and a sech-squared distribution. The final results quoted are for an exponential distribution in z which Wainscoat *et al.* (1989) found provided a good fit to stars in the edge-on galaxy IC 2531. Van Dokkum *et al.* (1994) obtain a similar result for NGC 6504. For the same scale-height, the sech-squared distribution produces a rotation curve with a peak $\sim 5\%$ higher.

For the vertical scale height, we explore a range of values (given in Table 7). The maximum expected value can be calculated from the observed velocity dispersion and the combined gaseous and stellar mass density, assuming verti-

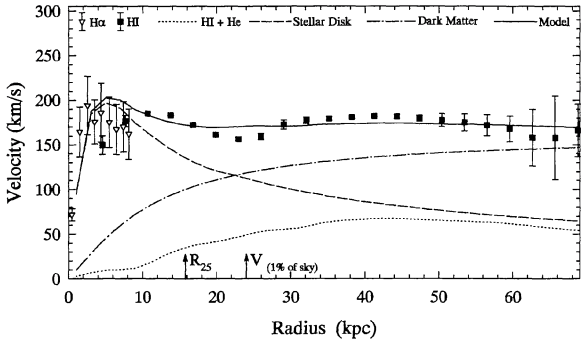

FIG. 11. Rotation curve models for NGC 289. The expected rotation due to the gaseous disk (dotted line), the best-fitting stellar disk with $M/L_I=2.13$ (dashed line) and the best–fitting halo of "dark matter" (dot–dash line) with $r_{\rm core}=9.77$ kpc and $\rho_0=0.0053$ $M_\odot$ pc^{-2} are shown, along with resulting complete model (solid line). Our re-analysis of the optical data from PB (triangles) and the full disk H I rotation curve (solid squares) are shown with "error bars" computed from the difference between the average rotation over the two sides of the disk (see text).

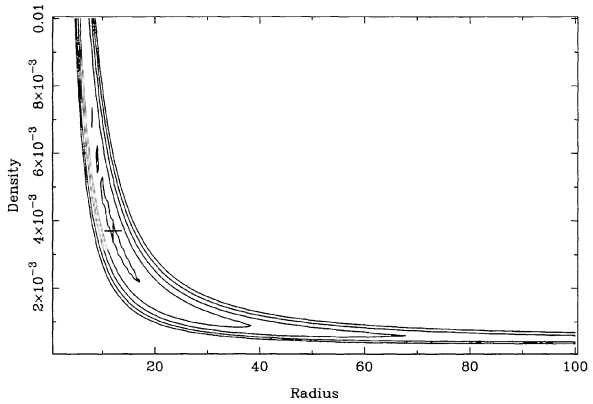

FIG. 12. Contour plot of χ^2 for the maximum disk fitting with $M/L_I=2.3$ and a disk thickness of 1.0 kpc, as a function of core radius (kpc) and halo central density ($M_\odot$ pc^{-2}). The cross indicates the minimum value of χ^2 for this model, which corresponds to a core radius of 12.0 kpc and a central density of 0.0037 $M_\odot$ pc^{-2}.

cal equilibrium (Camm 1950). Taking $\sigma\approx\sigma_z\sim12$ km s^{-1} (Fig. 10), and assuming a stellar mass-to-light ratio $M/L_I=2.3$ (see below), we expect a maximum scale height of ~1.8 kpc at radii less than ~35 kpc. Since the presence of a dark halo will tend to compress the disk (Olling 1995), the actual disk thickness will be lower. We reference our final results to a scale height $z_0=1$ kpc. This value is similar to that found by Olling & van Gorkom (1995) in their global model of NGC 4244.

We model the dark halo with a pseudo–isothermal sphere, although note that flattened halos may provide better fits to some data (Olling & van Gorkom 1995; Sackett & Pogge 1995). Following Casertano (1983), we use a halo with density profile,

$$\rho(r)=\frac{\rho_0}{1+(r/r_{\rm core})^2}, \tag{2}$$

which gives rise to a total enclosed mass:

$$M(r)=4\pi\rho_0[r_{\rm core}^2 r-r_{\rm core}^3\tan^{-1}(r/r_{\rm core})]. \tag{3}$$

For the model incorporating a halo and axisymmetric disk with a particular thickness and vertical distribution at the adopted distance, only the stellar M/L_I, halo core radius and halo central density remain free parameters. The best-fitting model suggests a stellar disk M/L_I of 2.1 ± 0.1, halo central density $\rho_0=0.0053\pm0.0019$ $M_\odot$ pc^{-3} and core radius 9.8 ± 2.1 kpc.

A conservative approach to the model fitting involves maximizing the contribution to the rotation due to the luminous disk (e.g. van Albada *et al.* 1985). Arguments considering the existence of the Tully–Fisher relationship and two-armed spiral structure as seen in NGC 289, together with stellar population models and the mass-to-light ratio in the local solar neighborhood suggest that a disk with close to the maximum mass-to-light ratio is appropriate for most spiral galaxies (Athanassoula *et al.* 1987; van der Kruit 1988). Beam smearing effects tend to lower the velocities observed in radio data and decrease the slope of the rotation curve in the inner part (Bosma 1978; Begeman 1989). For NGC 289, we are fortunate to have the high resolution Hα velocity measurements in the innermost regions as these provide an important constraint to the rotation velocities due to the luminous disk. The maximum permissible stellar mass-to-light ratio was found, for a disk exponential in z with constant scale height 1.0 kpc, by comparing rotation due to model disks with the observed rotation curve, to be $M/L_I\sim2.3$ (see Table 7). This M/L_I ratio can be compared with the predictions of population synthesis models (Arimoto & Yoshii 1986) which, for $U-B=0.1$, $B-V=0.7$ (RC3), and $V-I=0.8$ (present work), suggest that NGC 289 is a young (1–4 Gyr) object with approximately solar metallicity. The best–fitting population synthesis model predicts a high star formation efficiency for a Salpeter IMF, total luminosity and gas fractions similar to those observed, and $M/L_I\sim2.5$.

In Fig. 11 we add the PB data (triangles) to our measured rotation curve (solid squares with "error bars" as for the PB data points). The expected rotation due to gas (dotted line), maximum stellar disk (dashed line), a dark halo (dot-dash line) are shown along with the total model (solid line). Because of coupling between parameters, no statistically significant constraints can be placed on the halo core radius or central density with the present data. In Fig. 12 we plot χ^2 as a function of ρ_0 and core radius, for the maximum disk model with disk thickness 1.0 kpc; a cross marks the minimum of χ^2.

Figure 11 shows the "best-fitting" rotation curve model as determined by the nonlinear least-squares algorithm ($M/L_I=2.1$, $r_{\rm core}=9.77$ kpc, $\rho_0=0.0053$ $M_\odot$ pc^{-3}), although reasonable fits can be made in a wider range as suggested by Fig. 12. The halo shown contributes a mass of $\sim3.5\times10^{11}M_\odot$ for a stellar disk mass of $M_*\sim6.6\times10^{10}M_\odot$ and a gas mass of $M_{\rm HI}\sim3.6\times10^{10}M_\odot$. NGC 289, with $M_{\rm HI}/M_*\sim0.4$, is an extremely gas-rich system which requires a dark halo 3.5 times as massive as the stellar and gaseous components at the last measured point on the rotation curve.

7. SUMMARY AND DISCUSSION

The giant, LSB spiral galaxy NGC 289 has been observed in the V and I bands and using the 21 cm H I line. The optical images show that the galaxy has a small bulge, a small bar, and a high surface-brightness inner disk from which two regular spiral arms originate. The arms split into multiple components as they wind out into the very extended outer LSB disk and it is unclear from the morphology whether the galaxy is genuinely multiple-armed or a two-armed grand design spiral perturbed by its northerly dwarf elliptical companion. The outer disk is not well fitted by a single exponential, but has a shallow profile (with formal scale length of 5.4 kpc). The Parkes and ATCA observations show that the galaxy is gas rich, with $M_{\rm H\,I}/M_* \sim 0.4$. The measured H I disk extends to a radius of nearly 70 kpc where the surface density falls to a few times 10^{19} cm^{-2}. The optical disk in V reaches 1% of the sky level at 24 kpc. When logarithmic plots are compared, the azimuthally averaged radial H I density is flat as far as R_{25} whereas the stellar disk declines approximately exponentially in that region. The H I distribution is reasonably symmetric and clearly traces the outer spiral arms.

The first-moment velocity field was used in a standard tilted-ring analysis to derive the rotation curve. The residual velocity field and the comparison of the rotation curve with the position–velocity diagram show that the global kinematics are reasonably well described by circular motions. The rotation curve rises steeply to peak at 200 km s^{-1} and dips at a radius of 22 kpc to 156 km s^{-1} before rising and flattening at a level of $\sim$175 km s^{-1}. Within the uncertainties, there is no observed decline of the rotation curve at the last measured point.

To investigate the mass distribution, mass models consisting of gaseous and stellar disks plus a pseudo–isothermal spherical dark halo were considered. We find that a massive dark halo is required to fit the observed rotation curve. The best–fitting model has $M/L_I = 2.1 M_\odot/L_\odot$, $r_{\rm core} = 9.77$ kpc, $\rho_0 = 0.0053$ M$_\odot$ pc^{-3}, although the halo properties are coupled and not individually well constrained by the observations. As is the case in many other galaxies (Kent 1987; Freeman 1992, and references therein), the rotation curve due to the halo alone provides a reasonable fit to the observed rotation in the outer parts, making it impossible to disentangle the contributions due to the visible and dark matter and to find a unique form for the dark halo. In the best-fitting model, the halo mass is $\sim 3.5 \times 10^{11} M_\odot$, the total mass at the last measured point on the rotation curve is $\sim 4.7 \times 10^{11} M_\odot$ and the global mass-to-light ratio is 15.3.

We attempt to model the radial trend in kinematic parameters with a spiral density wave model and with a warped disk model. The warp model provides a satisfactory fit to the observed velocity field, but does not account for kinks seen in the isovelocity contours. A density wave model can also provide a reasonable fit beyond 12 kpc while reproducing some of the small-scale structure seen in the velocity field, but only if a leading spiral density wave (SDW) mode is invoked. There is no evidence for such a mode in the density distribution. This suggests that extra caution is required when analysing rotation curves of spiral galaxies with prominent spiral arms or in cases where the H I does not extend well past the optical radius. Some of the observable consequences of a SDW are indistinguishable from the effects of a warped disk, and it seems possible that some "kinematic warps" identified from features in observed velocity fields, such as twisting of the line of nodes, may, in fact, be partly the signature of the SDW. In NGC 289 it is possible that the spiral arms distort the velocity field in the inner parts, while a warp becomes increasingly pronounced at larger radii, but the present data do not allow us to separate the two effects.

Beyond the region where the spiral arms distort the velocity field in NGC 289, the rotation curve expected for the H I disk has a remarkably similar shape to the observed rotation curve. In NGC 289, as in many other gas-rich spirals (e.g., Jobin & Carignan 1990; Broeils 1992), the H I seems to be a very precise tracer of the mass distribution in the outer parts.

The uncertainty in the dark halo parameters due to the effect of the spiral structure on the rotation curve and the coupling of parameters means that we can only speculate on the relation of the halo to the dynamics and evolution of NGC 289. However, we note that NGC 289, like the Sc galaxy NGC 5963, has a high neutral gas content, a bright inner region surrounded by a large LSB disk, and an almost flat outer rotation curve (Romanishin *et al.* 1982), with asymptotic velocities of $\sim$175 km s^{-1} for NGC 289 and $\sim$130 km s^{-1} for NGC 5963 (Bosma *et al.* 1988). Both galaxies exhibit high nuclear [N II]/Hα ratios, with log [N II]/Hα = -0.14 for NGC 289 (Bonatto *et al.* 1989) and log[N II]/Hα = -0.16 for NGC 5963 (Romanishin *et al.* 1982), possibly suggesting a previous high rate of star formation in the central regions. NGC 5963's central lens has M/L typical of late type spirals ($M/L_B \sim 2$), but the global M/L climbs to $M/L_B \sim 18$ in the outer regions. For comparison, our best-fitting model finds $M/L_I \sim 2.1$ for NGC 289's stellar disk (which dominates the inner regions), and a global M/L of 15.3 for NGC 289. Bosma *et al.* (1988) analysis similar to ours, fit to NGC 5963 a dark matter halo with high central density ($\rho_0 = 0.042$ M$_\odot$ pc^{-3}) and relatively short core radius. NGC 289 and NGC 5963 both have $r_{\rm core}/R_{25} \sim 0.5$, compared to $r_{\rm core}/R_{25} \sim 3$ for the bright Sb-c galaxies NGC 801, NGC 6674, and NGC 7331 (Begeman 1987, Broeils 1992), suggesting the possibility that a deep potential well pulled both baryonic and halo material into the center of NGC 289 and NGC 5963, stimulating star formation there.

Figure 5 shows that, for NGC 289, the H I column density is enhanced in the vicinity of the outer optical spiral arms, which may indicate SDWs interfering or that the spiral density wave is particularly strong there. In a study of the spiral structure of another giant spiral galaxy, UGC 2885, Canzian *et al.* (1993) speculate that large spiral galaxies may be especially prone to strong density waves and that, in the outer parts of large galaxies, there is insufficient time for stellar encounters to heat the disk, leading to low local resistance to non-axisymmetric perturbations. At the last measured point on the rotation curve, NGC 289 has completed only six rotations in a Hubble time (independent of H_0), compared to an average of 15 rotations at $R_{\rm max}$ for 18 spirals in the

Broeils (1992) sample. The colors hint at even more extreme youth. Other LSB systems, such as Malin 1 (Impey & Bothun 1989), NGC 5963 (Bosma *et al.* 1988), the NE clump of H I 1225+01 (Giovanelli *et al.* 1991), and members of the Sprayberry *et al.* (1995b) sample also have outermost regions that have rotated fewer than 10 times in a Hubble time. A lower star formation rate in slowly rotating disks is consistent with numerical simulations of the growth of dense structures in galaxies with flat rotation curves. Palous *et al.* (1990) found that giant molecular cloud complexes can form naturally as gas swept up by expanding shells is concentrated by the differential rotation.

We thank Neil Killeen and Richard Gooch for help with AIPS, MIRIAD, and KARMA software. We thank Agris Kalnajs and Claude Carignan for many useful comments on earlier drafts of this paper. We acknowledge the use of Kor Begeman's ROCUR and ROTMOD programs in GIPSY. This research used the NASA/IPAC Extragalactic Database (Helou *et al.* 1991), which is operated by the Jet Propulsion Laboratory, Caltech, under contract with the National Aeronautics and Space Administration. W. M. W. acknowledges the support from an Australian Postgraduate Research Award through the University of New South Wales and the hospitality of the Australia Telescope National Facility.

REFERENCES

Arimoto, N., & Yoshii, Y. 1986, A&A, 164, 260
Arp, H. 1981, ApJS, 46, 75
Ashman, K. M. 1992, PASP, 104, 1109
Ashman, K. M., Persic, M., & Salucci, P. 1993, MNRAS, 260, 610
Athanassoula, E., Bosma, A., & Papaioannou, S. 1987, A&A, 179, 23
Australia Telescope 1992, J. Electron. Eng. Aust. Special Issue, Vol. 12, No. 2
Barnaby, D., & Thronson, Jr., H. A. 1994. AJ, 107, 1717
Beckman, J. E., & Cepa, J. 1990, A&A, 229, 37
Begeman, K. 1987, Ph. D. thesis, University of Groningen
Begeman, K. G. 1989, A&A, 223, 47
Bica, E., & Alloin, D. 1987, A&AS, 70, 281
Binney, J. 1978, MNRAS, 183, 779
Binney, J. 1992, ARA&A, 30, 51
Binney, J., & Tremaine, S. 1987, Galactic Dynamics (Princeton University Press, Princeton)
Bonatto, C., Bica, E., & Alloin, D. 1989, A&A, 226, 23
Bosma, A. 1978, Ph. D. thesis, University of Groningen
Bosma, A., van der Hulst, J. M., & Athanassoula, E. 1988, A&A, 198, 100
Bosma, A. 1991, in Warped Disks and Inclined Rings around Galaxies, edited by S. Casterano, P. D. Sackett, and F. Briggs (Cambridge University Press, Cambridge), p. 237
Bottema, R. 1996, A&A, 306, 345
Botinellli, L., Gouguenheim, L., Paturel, & Teerikorpi, P. 1986, A&A, 156, 157
Briggs, F. H. 1990, ApJ, 352, 15
Broeils, A. 1992, Ph. D. thesis, University of Groningen
Burstein, D., & Heiles, C. 1982, AJ, L87, 1165
Burton, W. B. 1971, A&A, 10, 76
Buta, R., & de Vaucouleurs, G. 1983, ApJS, 51, 149
Buta, R., Crocker, D. A., & Byrd, G. G. 1992, AJ, 103, 1526
Buta, R., & Williams, K. L. 1995, AJ, 109, 543
Buta, R. 1995, ApJS, 96, 39
Byrd, G. G., Freeman, T., & Howard, S. 1993, AJ, 105, 477
Camm, G. L. 1950, MNRAS, 110, 305
Canzian, B., Allen, R. J., & Tilanus, R. P. 1993, ApJ, 406, 457
Carignan, C., & Freeman, K. C. 1988, ApJ, 332, L33
Carignan, C., & Beaulieu, S. 1989, ApJ, 347, 760
Casertano, S. 1983, MNRAS, 203, 735
Condon, J. J. 1987, ApJS, 65, 485
Corbelli, E., Schneider, S. E., & Salpeter, E. E. 1989, AJ, 97, 390
Corbelli, E., & Salpeter, E. E. 1993, ApJ, 419, 104
de Jong, R. S. 1995, Ph.D. thesis, University of Groningen
de Vaucouleurs, G. 1979, ApJ, 227, 729
de Vaucouleurs, G., de Vaucouleurs, A., Corwin, H. G., Buta, R. J., Paturel, G., & Fouqué, P. 1991, Third Reference Catalogue of Bright Galaxies (Springer, New York) (RC3)
Devereux, N. 1987, ApJ, 323, 91
Dubinski, J., & Kuijken, K. 1994, ApJ, 442, 492
Elmegreen, D. M., & Elmegreen, B. G. 1987, ApJ, 314, 3
Fisher, J. R., & Tully, R. B. 1981, ApJS, 47, 139
Fouqué, P. 1984, A&AS, 55, 55
Freeman, K. C. 1992, in Physics of Nearby Galaxies, Nature or Nurture? edited by T. X. Thuan and C. Balkowski (J. T. T. Editions Frontieres, Gif-sur-Yvette), p. 201
Fridman, A. M. 1994, in Physics of the Gaseous and Stellar Disks of the Galaxy, ASP Conf. Ser. 66, edited by I. R. King (BookCrafters, San Francisco), p. 15
Giovanelli, R., Williams, J. P., & Haynes, M. P. 1991, AJ, 101, 1242
Giovanelli, R., Haynes, M. P., Salzer, J. J., Wegner, G., da Costa, L. N., & Freudling, W. 1994, AJ, 107, 2036
Graham, J. A. 1982, PASP, 94, 244
Helou, G., Madore, B.F., Schmitz, M., Bicay, M. D., Wu, X., & Bennett, J. 1991, The NASA/IPAC Extragalactic Database, in "Databases and On-Line Data in Astronomy," edited by D. Egret and M. Albrecht (Kluwer, Dordrecht)
Impey, C., & Bothum, G. 1989, ApJ, 341, 89
Irwin, J. A. 1995, PASP, 107, 715
Jobin, M., & Carignan, C. 1990 AJ, 100, 648
Kent, S. M. 1985, ApJS, 59, 115
Kent, S. M. 1987, AJ, 93, 816
Kraan-Korteweg, R. C. 1986, A&AS, 66, 255
Lake, G., & Feinswog, L. 1989, AJ, 98, 166
Lasker, B. M., Sturch, C. R., McLean, B. J., Russell, J. L., Jenkner, H., & Shara, M. M. 1990, AJ, 99, 2019
Lauberts, A., & Valentijn, E. A. 1989, The Surface Photometry Catalogue of the ESO-Uppsala Galaxies (ESO, Garching)
Lin, C. C., Yuan, C., & Shu, F. H. 1969, ApJ, 155, 721
Lindblad, P. O., & Lindblad, A. B. 1994, in Physics of the Gaseous & Stellar Disks of the Galaxy, ASP Conf. Ser. 66, edited by I. R. King (BookCrafters, San Francisco), p. 29
Maia, M. A. G., da Costa, L. N., & Latham, D. W. 1989, ApJS, 69, 809
Maloney, P. 1993, ApJS, 414, 41
Meurer, G. R., Carignan, C., Beaulieu, S. F., & Freeman, K. C. 1996, AJ, 111, 1551
Olling, R. P. 1995, AJ, 110, 591
Olling, R. P., & van Gorkom, J. H. 1995, in Dark Matter, AIP Conf. Proc. 336, edited by S. S. Holt and C. L. Bennett (American Institute of Physics, New York)
Palous, J., Franco, J., & Tenorio-Tagle, G. 1990, A&A, 227, 175
Pasha, I. I. 1985, SvAL, 11, 1
Pence, W. D., & Blackman, C. P. 1984, MNRAS, 210, 547
Persic, M. & Salucci, P. 1988, MNRAS, 234, 131
Puerari, I., & Dottori, H. A. 1992, A&AS, 93, 469
Reif, K., Mebold, U., Goss, W. M., van Woerden, H., & Siegman, B. 1982, A&AS, 50, 451
Rieke, G. H., & Lebofsky, M. J. 1985, ApJ, 288, 618
Romanishin, W., Strom, S. E., & Strom, K. M. 1982, ApJ, 258, 77
Rots, A. H. 1974, Ph. D. thesis, University of Groningen
Ryder, S. D, Staveley-Smith, L., Harding, P., & Boroson, T. A. 1995, AJ, 109, 1592

Sackett, P. D., Morrison, H. L., Harding, P., & Boroson, T. A. 1994, Nat, 370, 441
Sackett, P. D., & Pogge, R. W. 1995, in Dark Matter, AIP Conf. Proc. 336, edited by S. S. Holt and C. L. Bennett (American Institute of Physics, New York)
Sandage, A. 1993, ApJ, 402, 3
Schlosser, W., & Musculus, D. 1984, A&A, 131, 367
Seiden, P. E., & Gerola, H. 1979, ApJ, 233, 56
Sprayberry, D., Bernstein, G. M., Impey, C. D., & Bothun, G. D. 1995a, ApJ, 438, 72
Sprayberry, D., Impey, C. D., Bothun, G. D., & Irwin, M. J. 1995b, AJ, 109, 558
Staveley-Smith, L., & Davies, R. D. 1987, MNRAS, 224, 953
Tinsley, B. M. 1981, MNRAS, 194, 63
Toomre, A. 1983, in Internal Kinematics and Dynamics of Galaxies, IAU Symposium 100, edited by E. Athanassoula (Reidel, Dordrecht)
Tully, R.B., 1988, Nearby Galaxies Catalogue (Cambridge University Press, Cambridge)
Unger, S. W., Wolstencroft, R. D., Pedlar, A., Savage, A., Clowes, R. G., Leggett, S. K., & Parker, Q. A. 1989, MNRAS, 236, 425
van Albada, T. S., Bahcall, J. N., Begeman, K., & Sancisi, R. 1985, ApJ, 295, 305
van der Hulst, J. M., Skillman, E. D., Smith, T. R., Bothum, G. D., McGauth, S. S., & de Blok, W. J. G. 1993, AJ, 106, 548
van der Kruit, P. C. 1988, A&A, 192, 117
van Dokkum, P. G., Peletier, R. F., de Grijs, R., & Balcells, M. 1994, A&A, 286, 415
van Gorkom, J. H. 1993, in The Environment and Evolution of Galaxies, edited by J. M. Shull and H. A. Thronson, Jr. (Kluwer, Dordrecht), p. 345
Véron-Cetty, M.-P. 1984, A&AS, 58, 665
Véron-Cetty, M.-P., & Véron, P. 1986, A&AS, 66, 335
Vorontsov-Velyaminov, B. A. 1977, A&AS, 28, 1
Wainscoat, R. J., Freeman, K. C., & Hyland, A. R. 1989, ApJ, 337, 163
Waterbos, R. A. M., Braun, R., & Kennicutt, Jr., R. C. 1994, AJ, 107, 184